High Resolution Acoustic Imaging of Laboratory Rock Samples Using Full Waveform Inversion

Farnoush Forghani[1*], *Jyoti Behura*[1,2], *Manika Prasad*[1], *Guenter Fuchs*[3]
[1] *Colorado School of Mines,* [2] *Seismic Science LLC,* [3] *Fuchs Consulting*

Corresponding author's email: fforghan@mines.edu

Keywords

Full waveform inversion, Acoustic imaging, Tomography, Gradients, Source-receiver spacing, Cycle-skipping.

Summary

High resolution elastic imaging of laboratory rock/core samples can provide valuable information about the quantitative small-scale physio-chemical changes including stress changes and fluid flow.

Here, we present the application of 3D Full Waveform Inversion, a high resolution imaging technique, to a laboratory acoustic data that we acquired with high spatial ultrasound source-receiver distribution. Using a 3D Full Waveform Inversion, we obtained a high resolution image of the laboratory shale sample. We also present our learnings on the importance of key parameters in obtaining reliable images by Full Waveform Inversion.

Introduction

Ultrasound laboratory experiments on core samples can provide insights into the local elastic properties (P- and S- wave velocities, and attenuation) of geological structures and reveal information on anisotropy, heterogeneity, and fluid flow in those targeted structures (Prasad, 2003; Adam & Otheim, 2013). Moreover, time-lapse monitoring of core samples can reveal valuable information on change of rock physics properties in a geological structure due to stress changes and fluid injection, or extraction (Prasad & Manghnani, 1997; Vialle & Vanorio, 2011).

Conventional ultrasound experiments commonly use a limited number of transmitted arrival times (mostly along two perpendicular azimuths in a sample), therefore, because of the incomplete spatial sampling of the wavefield are only able to determine the bulk P- and S-wave velocities and their azimuthal variations along the measured wavefields Shragge *et al.* (2015). While bulk elastic velocities are informative, they can not represent the quantitative small-scale physical properties of a structure. More sophisticated imaging techniques such as tomography, migration, and Full Waveform Inversion are needed to provide the quantitative elastic properties as a function of space.

In their feasibility study, Shragge *et al.* (2015) show the capability of Laser Ultrasound in providing sufficient spatial sampling of acoustic wavefield. They are able to obtain a high resolution acoustic image of a millimeter-scale fracture structure using Reverse Time Migration (RTM).

Application of Full Waveform Inversion (FWI) to seismic field data has clearly demonstrated its high resolution as the advantage to other imaging techniques (Brenders & Pratt, 2007a,b; Brossier *et al.*, 2009; Pratt *et al.*, 1998; Pratt, 1999; Sirgue *et al.*, 2007; Takougang & Calvert, 2012; Tape *et al.*, 2009). As of our knowledge, there is no existing study of application of FWI to laboratory rock samples.

We applied the 3D FWI to an acoustic data that we recorded on a laboratory shale sample at high spatial sampling by ultrasound (megahertz frequencies) piezoelectric transducers as sources and receivers. We investigated the importance of source-receiver spacing, frequency content, and the receiver aperture in obtaining reliable FWI images.

FWI Methodology

FWI is a nonlinear inversion (Lailly, 1984; Tarantola, 1984), where the full information content in the seismogram can be considered in an optimization process to obtain a model of the physical-properties that best match the acquired data. Like any other inversion technique, FWI works by minizing the misfit between recorded and modeled data, also called as the objective function (Nocedal & Wright, 2006; Virieux & Operto, 2009). The gradient of the least-squares objective function is efficiently computed using the adjoint-state method as described in Tromp *et al.* (2005); Askan (2006); Plessix (2006); Liu & Tromp (2006).

We can summarize the FWI main steps as follows:

1. The first step is to simulate/predict the direct acoustic arrivals using a forward modeling algorithm. The forward modeling algorithm uses the wave equation and an initial velocity model to generate predicted data. The initial velocity is a guess based on the information about our material. A traveltime-tomography-derived model may be used as the initial model.

2. The second step comprises of computation of the objective function and it's gradient with respect to the model parameters. Here, we use the normalized $l-2$-norm of the difference between the computed and observed data as the objective function.

3. In the final step, the model is updated after computing a proper step-length.

4. The above three steps are repeated iteratively until a termination criterion is fulfilled. We stop the iter-

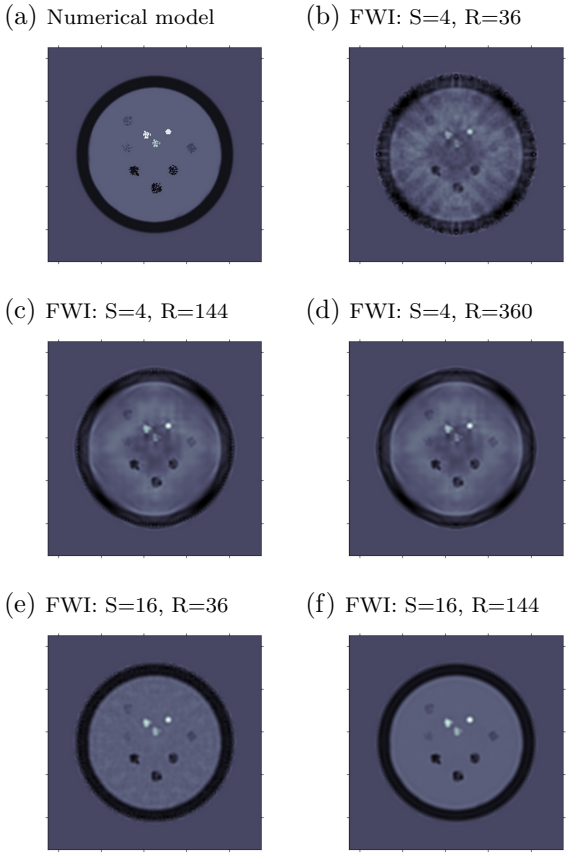

Fig. 1: a) Numerical sample, b)–f) FWI results for different numbers of sources (S) and receivers (R). All images are displayed using the same color scale

ations when the gradient falls below a tolerance or the objective function becomes sufficiently small.

Determination of Acquisition Parameters

Figure 1 shows the acoustic FWI of a numerical sample for various acquisition geometries (with central frequency of 1 MHz). The true velocity model is shown in Figure 1a. The small spots inside the circle represent different heterogeneities inside the sample. The initial velocity model is the background velocity and does not contain any of the heterogeneities. Comparison of Figures 1a and 1f shows that by using 16 sources and 144 receivers uniformly distributed across the sample, this numerical sample can be accurately (qualitatively and quantitatively) imaged. Note that in this example even the receiver locations with 10° angular intervals (Figure 1e) provide sufficient resolution in the FWI image.

Laboratory Data

We acquired an acoustic ultrasound dataset on a cylindrical shale sample with a 10 cm diameter and 6 cm thickness (Figure 2). To create a controlled heterogeneity

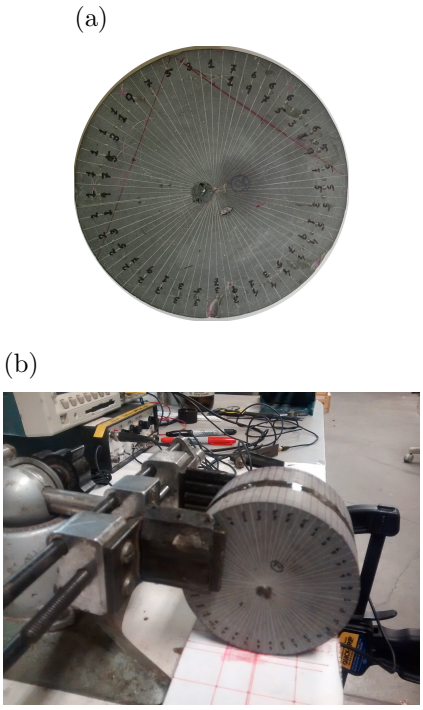

Fig. 2: a) Plan view of the Shale sample used for the ultrasound acoustic experiment. The diameter of the sample is 10 cm with a heterogeneity of 4 mm in diameter at the left of its center; b) Experimental set up for ultrasonic data collection for FWI imaging. The shiny stripe in the middle of the sample is an acoustic couplant and indicates the section of the sample where we positioned our receiver transducers. The source transducer is stabilized inside a wood plate underneath the sample.

that can be imaged by FWI, we drilled a 4 mm diameter hole inside the sample. We filled up the hole with epoxy to avoid large contrasts that generate waveform complexities. Figure 3 illustrates the acquired ultrasound waveforms in twenty source gathers. Among the arrivals in Figure 3, one can see the acoustic direct/transmitted arrivals around 45 microseconds and the surface-wave arrivals (criss-crossing events) around 75 microseconds.

Figure 4 shows a zoom of the direct/transmitted arrivals that is used for FWI with the corresponding source-receiver aperture overlaid on each source gather. The Fourier transform in the bottom panel of Figure 4 shows the frequency content of the data is in 0.2-1 MHz range.

Analysis of FWI of Laboratory Data

We separated the direct acoustic arrivals from the rest of the arrivals (arrivals shown in Figure 4) and used them as input to the FWI algorithm. We then estimated the source signature using the deconvolution technique of Pratt (1999). We used a homogeneous initial velocity of 3350 m/s based on the bulk acoustic velocity in shale.

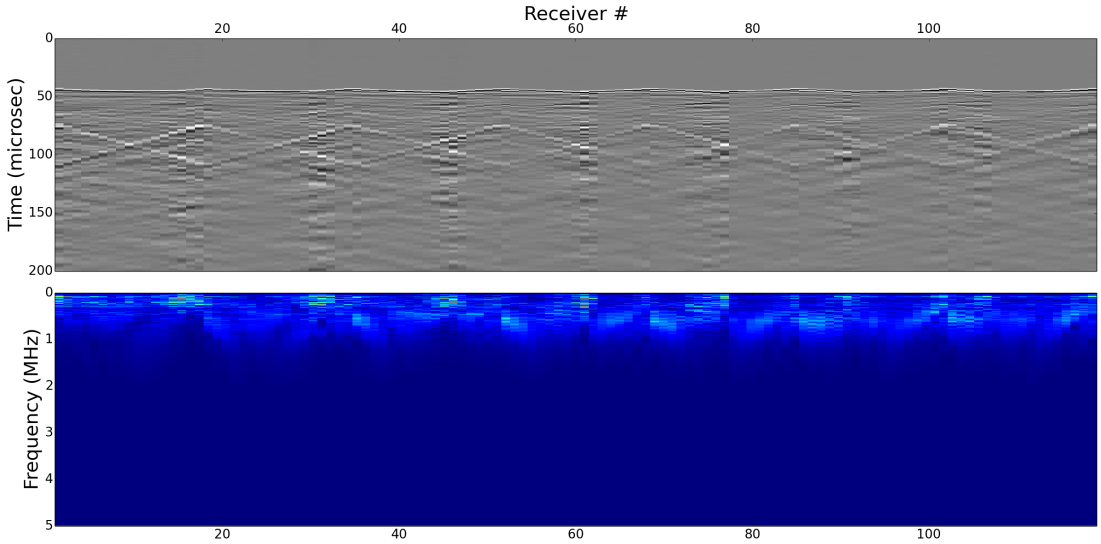

Fig. 3: Top) ultrasound laboratory data acquired on the shale sample; data is collected in twenty source gathers (seven of the source gathers are illustrated here). Each source gather includes seventeen receivers. In each gather the source location on the left half of the sample moves counter-clockwise from the top of the sample towards the bottom of the sample. The source spacing is 10° and the receiver spacing is 5°; x-axis and y-axis correspond to the receiver number and arrival time in microsecond, respectively. bottom) Fourier transform of the data in the top panel. x-axis and y-axis correspond to the receiver number and frequency in MHz, respectively.

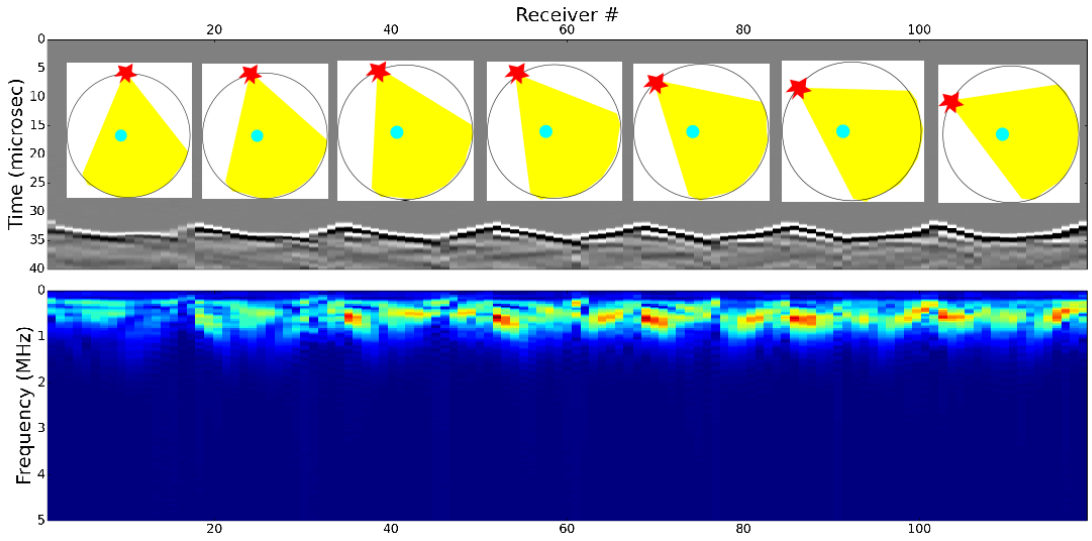

Fig. 4: A zoom of Figure 3; top) Seven source gathers (only the direct arrivals are shown). Each gather is overlaid by schematic illustration of the source location (marked by a red star) and receiver aperture of about 80° (shown in yellow circular sector); the cayon circle indicates the hole (heterogeneity). x-axis and y-axis correspond to the receiver number and arrival time in microsecond, respectively. bottom) Fourier transform of the data in the top panel. x-axis and y-axis correspond to the receiver number and frequency in MHz, respectively.

We then obtained the first iteration gradients using all the frequencies in the data shown in Figure 5. As gradients represent changes that need to be applied to our initial velocity model, with a successful FWI process, the first iteration gradient image should be similar (in pattern) to the final acoustic image that we aim to obtain.

The velocity gradient image in Figure 5 involves very important information that are listed below:

- The hole filled with epoxy is visible in the velocity gradients. Note that gradient image is not the velocity image but shows where velocity needs to be altered with respect to the input velocity model in order to reduce the data misfit.

- The footprint of insufficient source and receiver spacing is visible in the gradient image. On the left half of the gradient image we can see the oval shaped artifacts due to insufficient source spacing (10°). On the right half of the gradient image these artifacts are smaller and less intense due to the smaller receiver spacing (5°). Note that the synthetic test suggested that the receiver spacing of 10° is sufficient to recover the true model. However, in the synthetic example, for each source gather we used the whole receiver aperture (360°), whereas in our laboratory sample, only 80° receiver apertures were used. We are currently analyzing the sensitivity kernels to obtain an in-depth understanding of the role of source- and receiver-spacing and receiver aperture in FWI (Fichtner & Trampert, 2011; Tromp *et al.*, 2005). Our initial estimates (based on the size of the first Fresnel zone) suggest the receiver aperture of 80° is not sufficient. The data acquisition with receiver aperture of 270° is in progress.

Cycle-skipping is a common problem in performing FWI (Virieux & Operto, 2009) that can result in inaccurate velocity images. (Virieux & Operto, 2009) explain that because low frequencies are less sensitive to cycle-skipping, a successive multiscale inversion with increasing high-frequency content will reduce the cycle-skipping artifacts. To reduce the cycle-skipping, we followed the strategy of Bunks *et al.* (1995) and Sirgue & Pratt (2004) and performed the multiscale approach of successive inversion starting at 0.2 MHz and increasing the frequency content up to 1 MHz.

Figure 6 illustrates the 6th iteration velocity image by FWI using data with all frequencies (0.2-1 MHZ). We can see the location and resolution of the heterogeneity/hole is accurately recovered in this image. There are some artifacts in the image that are due to insufficient source-spacing and receiver-spacing, and some due to incomplete receiver aperture. We anticipate to observe suppression of artifacts due to receiver-aperture in the image of the data that we are currently acquiring with larger receiver aperture of 270°. One can also see other features in the image that might be related to the natural heterogeneity of the shale sample. Further investigation of these heterogeneities can be obtained by comparison of the images obtained from 80° and 270° receiver apertures.

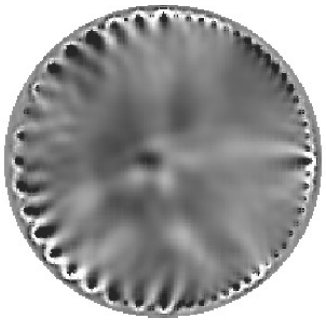

Fig. 5: First iteration velocity gradients calculated for all the frequencies of the data in Figure 4. In the gray color scale, dark areas indicate negative and light areas indicate positive gradients ranging from -2.0×10^{-9} to 2.0×10^{-9}.

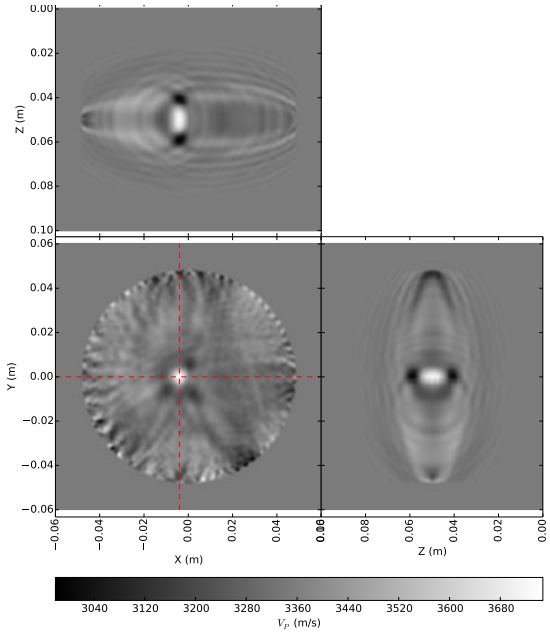

Fig. 6: The 6th iteration 3D velocity image obtained by FWI using data with all frequencies (0.2-1 MHZ). Top panel shows the velocity image in x-z plane, while bottom left and bottom right panels illustrate the velocities in x-y and y-z planes, respectively.

Conclusions

We applied 3D FWI to a laboratory acoustic data acquired on a shale sample. Our results show that high resolution imaging of laboratory samples by ultrasound data is feasible. Our learnings on the importance of key parameters in obtaining reliable FWI images are as follows:

- Insufficient source and receiver spacing and incomplete receiver aperture result in artifacts in the images.
- Incorrect initial model can cause cycle-skipping that result in inaccurate imaging. A multiscale approach of successive inversion of low to high-frequency content data will reduce the cycle-skipping effects.
- Although the shale sample appears homogeneous to the eye, it is clear from the gradient image as well as the FWI result that the sample is heterogeneous at the scale of ultrasound wavelength.

References

Adam, L., & Otheim, T. 2013. Elastic laboratory measurements and modeling of saturated basalts. *Journal of Geophysical Research*.

Askan, A. 2006. *Full waveform inversion for seismic velocity and anelastic losses in heterogeneous structures*. Ph.D. thesis, Carnegie Mellon University.

Brenders, A. J., & Pratt, R. G. 2007a. Efficient waveform tomography for lithospheric imaging: implications for realistic, two-dimensional acquisition geometries and low-frequency data. *Geophysical Journal International*, **168**(1), 152–170.

Brenders, A. J., & Pratt, R. G. 2007b. Full waveform tomography for lithospheric imaging: results from a blind test in a realistic crustal model. *Geophysical Journal International*, **168**(1), 133–151.

Brossier, Romain, Operto, Stéphane, & Virieux, Jean. 2009. Seismic imaging of complex onshore structures by 2D elastic frequency-domain full-waveform inversion. *Geophysics*, **74**(6), WCC105–WCC118.

Bunks, C., Saleck, F. M., Zaleski, S., & Chavent, G. 1995. Multiscale seismic waveform inversion. *GEOPHYSICS*, **60**(5), 1457–1473.

Fichtner, Andreas, & Trampert, Jeannot. 2011. Hessian kernels of seismic data functionals based upon adjoint techniques. *Geophysical Journal International*, **185**(2), 775–798.

Lailly, P. 1984. The seismic inverse problem as a sequence of before stack migrations. *Pages 206–220 of: Abstracts*. Society of Industrial and Applied Mathematics.

Liu, Q., & Tromp, J. 2006. Finite-Frequency Kernels Based on Adjoint Methods. *Bulletin of the Seismological Society of America*, **96**(6), 2383–2397.

Nocedal, J., & Wright, S. J. 2006. *Numerical Optimization*. 2nd edn. New York: Springer.

Plessix, R.-E. 2006. A review of the adjoint-state method for computing the gradient of a functional with geophysical applications. *Geophysical Journal International*, **167**(2), 495–503.

Prasad, M., & Manghnani, M. H. 1997. Effects of pore and differential pressure on compressional wave velocity and quality factor in Berea and Michigan sandstones. *Geophysics*.

Prasad, Manika. 2003. Velocity-permeability relations within hydraulic units. *Geophysics*.

Pratt, G., Shin, C., & Hicks, G. J. 1998. Gauss Newton and full Newton methods in frequency space seismic waveform inversion. *Geophysical Journal International*, **133**(2), 341–362.

Pratt, R. Gerhard. 1999. Seismic waveform inversion in the frequency domain, Part 1: Theory and verification in a physical scale model. *Geophysics*, **64**(3), 888–901.

Shragge, Jeffrey, Blum, Thomas E., van Wijk, Kasper, & Adam, Ludmila. 2015. Full-wavefield modeling and reverse time migration of laser ultrasound data: A feasibility study. *Geophysics*.

Sirgue, L., & Pratt, G. 2004. Efficient waveform inversion and imaging: A strategy for selecting temporal frequencies. *Geophysics*, **69**(231).

Sirgue, Laurent, Etgen, John, & Albertin, Uwe. 2007. 3D full-waveform inversion: Wide- versus narrow-azimuth acquisitions. *SEG Technical Program Expanded Abstracts*, **26**(1), 1760–1764.

Takougang, E. M. Takam, & Calvert, A. J. 2012. Seismic velocity and attenuation structures of the Queen Charlotte Basin from full-waveform tomography of seismic reflection data. *Geophysics*, **77**(3), B107–B124.

Tape, C., Liu, Q., Maggi, A., & Tromp, J. 2009. Adjoint Tomography of the Southern California Crust. *Science*, **325**(5943), 988–992.

Tarantola, A. 1984. Inversion of seismic reflection data in the acoustic approximation. *Geophysics*, **49**(8), 1259–1266.

Tromp, J., Tape, C., & Liu, Q. 2005. Seismic tomography, adjoint methods, time reversal and banana-doughnut kernels. *Geophysical Journal International*, **160**(1), 195–216.

Vialle, S., & Vanorio, T. 2011. Laboratory measurements of elastic properties of carbonate rocks during injection of reactive CO2 -saturated water. *Geophysical Research Letters*.

Virieux, J., & Operto, S. 2009. An overview of full-waveform inversion in exploration geophysics. *Geophysics*, **74**(6), WCC1–WCC26.

Acknowledgements

We thank Ramona Graves, Dean of the College of Earth Resource Sciences & Engineering, Kevin Moore, Dean of the College of Engineering and Computational Sciences, Michael Kaufmann, Dean of the College of Applied Science and Engineering, and Anthony Dean, the VP of the Research and Technology Transfer at Colorado School of Mines for providing funding for this research. We thank Geoff Brennecka and Michael Wakin at Colorado School of Mines for providing technical feedback. We thank the High Performance Computing center at Colorado School of Mines for providing computational resources. We are also thankful to Cesar Mapeli, Andre Panfiloff, Azar Hasanov, Rowdy Mathews, Manju Murugesu, and Mandy Schindler at Rock Physics Lab at Colorado School of Mines for their help with the experimental set up.